Advanced Materials

ADVANCED MATERIALS
www.advmat.de

RESEARCH ARTICLE OPEN ACCESS
Rising Stars

Photo-Rewritable Ambipolar Organic Electrochemical Synapses with Bidirectional Optical Plasticity for Adaptive Vision in Aqueous Environments

Xiaoqian Su[1,2] | Xihu Wu[1] | He Wang[3] | Wenzhe Lu[1] | Bing Xue[2,4] | Jinli Tang[1] | Zhangshanhao Li[4] | Kejing Ren[4] | Qiang He[1] | Junyu Li[5] | Lan Yin[6] | Yuxin Liu[2,7,8] | Shiming Zhang[9] | Ting Lei[10] | Changsheng Wu[2,3,4,8]

[1]Institute of Flexible Electronics (IFE, Future Technologies), Xiamen University, Xiamen, China | [2]Institute for Health Innovation and Technology, National University of Singapore, Singapore, Singapore | [3]Department of Electrical and Computer Engineering, National University of Singapore, Singapore, Singapore | [4]Department of Materials Science and Engineering, National University of Singapore, Singapore, Singapore | [5]Sinopec Shanghai Research Institute of Petrochemical Technology, Shanghai, China | [6]School of Materials Science and Engineering, The Key Laboratory of Advanced Materials of Ministry of Education, State Key Laboratory of Flexible Electronics Technology, Tsinghua University, Beijing, China | [7]Department of Biomedical Engineering (BME), National University of Singapore, Singapore, Singapore | [8]The N.1 Institute for Health, National University of Singapore, Singapore, Singapore | [9]Electrical and Electronic Engineering, The University of Hong Kong, Hong Kong, China | [10]National Key Laboratory of Advanced Micro and Nano Manufacture Technology, School of Materials Science and Engineering, Peking University, Beijing, China

Correspondence: Changsheng Wu (cwu@nus.edu.sg)

Received: 31 August 2025 | **Revised:** 21 March 2026 | **Accepted:** 24 March 2026

Keywords: ambipolar | artificial vision | bulk heterojunction | organic electrochemical transistors | photo-rewritable synapse

ABSTRACT

Emulating biological vision requires aqueous-compatible neuromorphic devices that perform light sensing and complex synaptic dynamics. Organic electrochemical transistors (OECTs), capable of converting ionic signals into electronic current via electrochemical doping, closely mimic biological synaptic signaling. This capability distinguishes them from traditional electronic synapses, which rely purely on electron transport. However, prior OECTs typically require multiple components for bidirectional synaptic potentiation and depression, limiting integration and scalability. Here, we present an ambipolar all-polymer bulk heterojunction vertical OECT that enables light-tunable bidirectional synaptic plasticity while functioning stably in aqueous electrolytes at low operating voltages (≤ 0.4 V). Through photon-modulated electrochemical doping and ambipolar charge transport, the device integrates light sensing, bidirectional synaptic plasticity, and sustained memory (over 130 min) in a single device, mimicking the dual-polarity signaling of retinal bipolar cells. This design allows the transistor to read, write, and erase signals without complex external circuitry. We further demonstrate a vertically integrated optoelectronic synaptic array capable of image recording, selective optical erasure, rewriting, and background denoising, highlighting the feasibility of both global and localized reprogramming. This scalable, light-controlled organic synapse unlocks high-density, biocompatible circuits for artificial retinas and neuromorphic vision.

Xiaoqian Su and Xihu Wu contributed equally to this work.

1 | Introduction

Photoelectronic synapses, capable of perceiving and storing visual information, hold great promise for artificial visual sensory systems [1–3]. In biological systems, the retina performs highly complex visual signal preprocessing by converting optical stimuli into neural activity through ionic signaling within a fluidic environment. Central to this process are synaptic connections between neurons that enable sophisticated information processing. Therefore, replicating such advanced perception in artificial systems necessitates neuromorphic devices that integrate light detection (as sensing), dynamic synaptic plasticity (for learning and memory), and biomimetic ionic signaling (for energy-efficient operation), thereby enabling adaptive, low-power, and human-like sensory processing capabilities [4–7].

While traditional artificial photoelectronic synapses, including those based on silicon and other inorganic materials, have significantly advanced the field of neuromorphic optoelectronics [8–12], their operation fundamentally relies on electronic charge transport, which differs markedly from the ion-regulated modulation seen in biological neurons [4, 13]. In contrast, within the retinal phototransduction cascade, ions act as critical signal carriers, facilitating the energy-efficient conversion of optical stimuli into electrical signals. The retina uniquely employs ion-specific properties to achieve remarkable visual processing, including color perception, contrast enhancement, and motion detection. These ion-based processes enable inherently low-energy transport, typically requiring only tens of millivolts [14] (significantly lower than the voltages needed for purely electronic charge transport [15–18]), while also providing excellent biocompatibility and allowing complex signal modulation through variations in ionic concentration, ion type, and gating. Mimicking these ion-regulated mechanisms is thus paramount for next-generation artificial photoelectronic synapses to overcome limitations in energy efficiency, bio-integration, and dynamic adaptation, thereby enabling more sophisticated and biologically relevant visual perception [19–21].

Organic electrochemical transistors (OECTs) have emerged as highly promising components for bio-inspired artificial synapses, offering a unique combination of ionic and electronic conduction, low-voltage operation, and inherent biocompatibility, which makes them well-suited for interfacing with biological systems [22, 23]. This mixed-conduction mechanism closely mimics biological synapses, providing a bio-inspired route to emulating efficient and nuanced signal transduction [24–27]. Recent advances in OECT-based artificial synapses have yielded innovative designs and functionalities that more closely mirror the complexity of neural networks, enabling parallel, fault-tolerant, and energy-efficient artificial neural networks capable of tasks such as pattern recognition, motor control, and multisensory integration [26, 28]. More recently, the integration of optoelectronics functionality has endowed OECTs with light-sensing capabilities suitable for visual preprocessing and image-based learning [4, 29, 30]. However, existing OECT designs often exhibit unidirectional plasticity, enabling optical potentiation but relying on external gating for depression. As a result, they lack the dynamical bidirectional adaptability observed in biological circuits, particularly the dual-polarity signaling of retinal bipolar cells, which balances potentiation and suppression in retina-inspired visual processing. In neuromorphic hardware, achieving such dual-mode optical functionality within a single synaptic unit could drastically simplify synaptic array design by enabling both memory writing and erasing in the same element, thereby reducing the need for selector transistors and multiple control terminals.

Here, we report an ambipolar synaptic platform based on a vertically integrated all-polymer bulk heterojunction (BHJ) that enables photoresponsive, bidirectional synaptic plasticity and operates reliably in aqueous environments. The BHJ consists of *p*-type (poly[6-methyl-pyrrolo[3,2-*b*:4,5-*b*′]bis-[1,4]benzothiazine], PBBT-Me) and *n*-type (poly(benzimidazobenzophenanthroline), BBL) ladder-type polymers, enabling ambipolar charge transport, light-regulated ionic-electronic modulation, and non-volatile memory retention exceeding 130 min in PBS, which is remarkable for aqueous systems. Notably, both excitatory and inhibitory synaptic functions are achieved optically under different gate biases, without modifying the circuit or applying additional electrical erasing pulses, such that a single device can perform excitation, inhibition, read, write, and erase functions. We further demonstrate a 10 × 10 synaptic array capable of optical image recognition, storage, selective erasure, denoising, and dynamic reconfiguration through spatially controlled light stimulation. Overall, this ion-based synaptic device enables stable biologically relevant spiking dynamics in aqueous environments at frequencies comparable to those of biological neurons, advancing bio-inspired, scalable neuromorphic visual processing systems and paving the way for seamless integration with biological systems.

2 | Results and Discussion

2.1 | Overview of a Bioinspired Adaptive Organic Photoelectrochemical Synapse

The human visual system processes optical information through retinal neurons that dynamically encode light stimuli into electrical impulses through excitatory and inhibitory synaptic signaling via ion flux-driven synaptic activity in an aqueous environment (Figure 1a). Retinal bipolar cells, in particular, process both positive and negative contrast signals via dual-polarity neurotransmitter responses, enabling essential visual functions such as edge detection, motion tracking, and contrast adaptation [31, 32]. Replicating these capabilities in artificial systems requires synaptic devices that not only respond to light but also support bidirectional plasticity under physiologically relevant conditions.

To emulate this fundamental feature of visual processing, we developed an organic photoelectrochemical synapse that integrates light perception, signal transduction, and memory storage within a monolithic platform compatible with aqueous operation (Figure 1b). Our device is based on a vertical organic electrochemical transistor (vOECT) structure employing an ambipolar bulk heterojunction (BHJ) composed of a *p*-type ladder polymer (PBBT-Me) and an *n*-type ladder-conjugated polymer (BBL). The *n*-type and *p*-type ladder-conjugated polymer BBL and PBBT-Me are selected for their complementary electronic properties

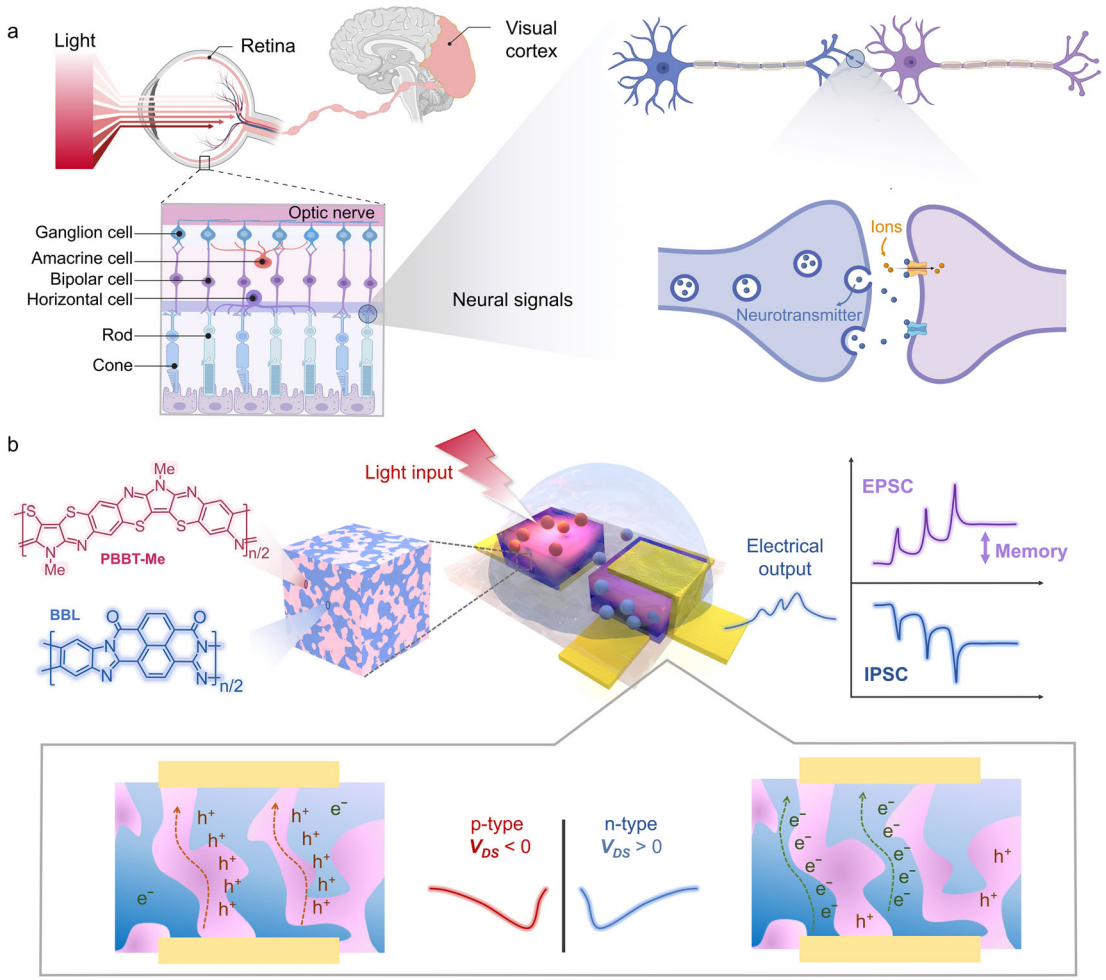

FIGURE 1 | Overview of the biological visual system and BHJ vOECT-based artificial visual system. (a) Schematic of the human visual system illustrating optical information captured by retinal neurons and its conversion into neural signals for transmission to the brain through ion flux-driven synaptic activity. (b) Schematic of the photoelectrochemical synaptic device architecture featuring an ambipolar BHJ composed of PBBT-Me and BBL materials. This all-polymer BHJ enables ambipolar charge transport and photon-modulated electrochemical doping, achieving bidirectional conductivity modulation essential for mimicking the bipolar characteristics of retinal cells. V_{DS} represents drain-source voltage.

[33, 34], strong visible-light absorption [34], and electrochemical stability in aqueous media, enabling balanced ambipolar transport [35]. The device demonstrates light absorption and photo-modulated electrochemical doping processes that emulate photoreceptor and bipolar cell functions with excitatory and inhibitory responses. Upon light exposure, excitons generated within the BHJ are separated and stabilized by gate-induced ion migration, giving rise to bidirectional synaptic behavior. Excitatory postsynaptic current (EPSC) is observed when the absolute value of the postsynaptic current (|PSC|) increases with pulse application, while inhibitory postsynaptic current (IPSC) occurs when |PSC| decreases, which mimics excitatory and inhibitory neurotransmission, respectively. Crucially, all operations are conducted under low voltage (≤0.4 V) in phosphate-buffered saline, mimicking the ionic environment of neural tissue.

2.2 | *n*-type Photoelectrochemical Synaptic Device

To realize bidirectional synaptic behavior in our photoelectrochemical device, understanding the individual characteristics of *n*- and *p*-type components is essential. We first investigated the photosensitive electrochemical properties of the *n*-type BBL film (Figure 2a). In situ UV–vis absorption measurements of the BBL film in PBS electrolyte revealed strong absorption in the range of 350–700 nm with a peak centered at 580 nm (Figure S1). As the bias was progressively increased, cations from the PBS electrolyte entered the BBL film, resulting in a gradual decrease in the absorption peak around 580 nm and the emergence of new absorption features beyond 700 nm (corresponding to polaron transitions in BBL). These changes in the absorption spectra directly reflect modifications in the film's electronic band structure and indicate efficient electrochemical doping. Specifically, the spectral evolution demonstrates that the BBL film is electrochemically doped by the injected ions, transitioning from a neutral to a reduced state and undergoing charge accumulation. Cyclic voltammetry (CV) tests revealed that the reduction onset potential of BBL in PBS is 0.09 V, with a reduction peak at −0.47 V, indicating an electrochemical reaction during its electron-accepting process (Figure 2b and Figure S2). Under illumination at a specific wavelength (typically 660 nm unless otherwise specified), both the onset potential and reduction peak

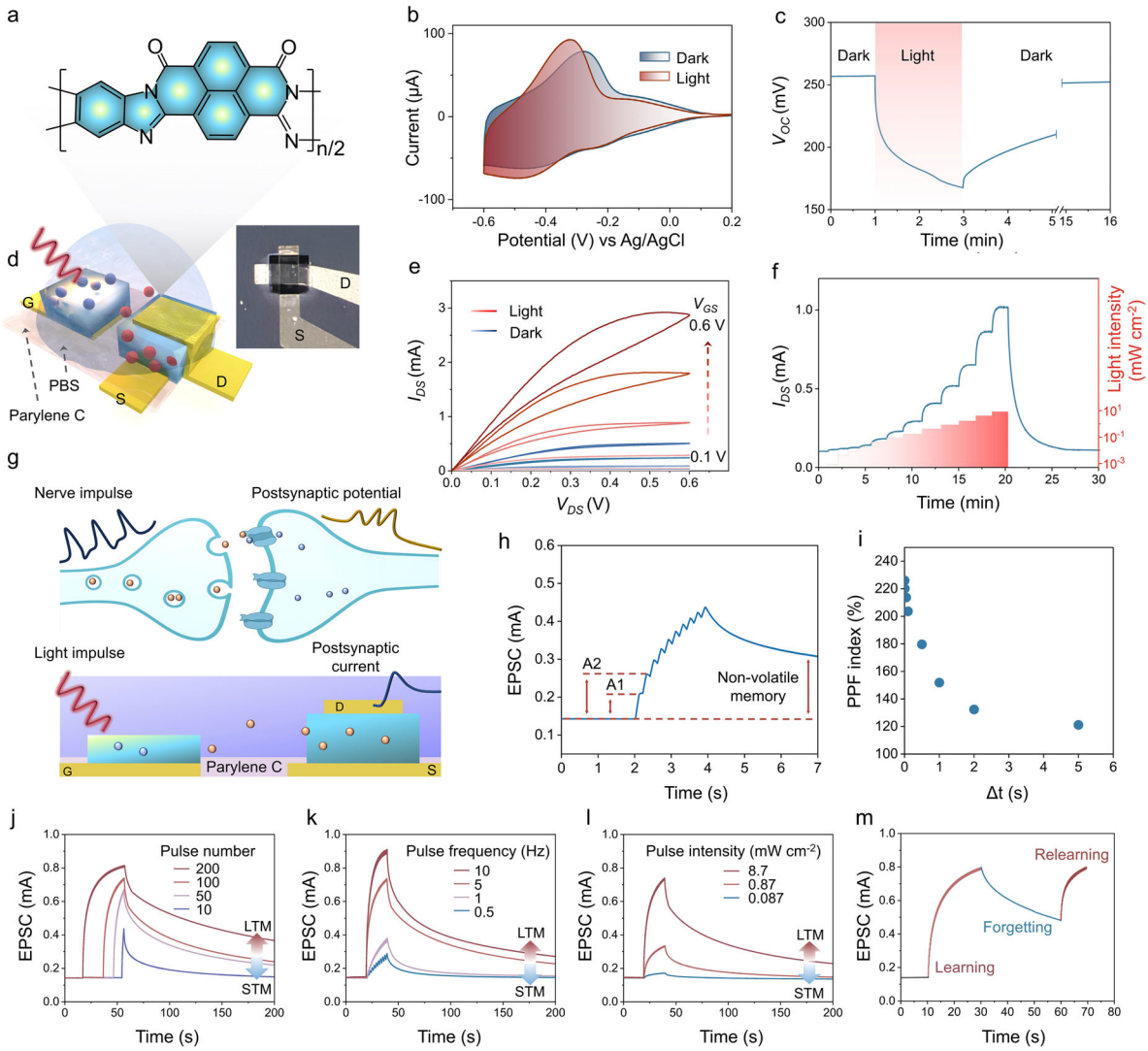

FIGURE 2 | Characterization of BBL-based *n*-type photoelectrochemical synaptic device. (a) Chemical structure of BBL, an *n*-type ladder conjugated polymer. (b) Cyclic voltammetry (CV) curve of BBL in the dark and under illumination. (c) Open-circuit voltage (V_{OC}) of the BBL film in the dark and under illumination. (d) Schematic of BBL-vOECT device configuration, featuring bottom (source, 100 μm) and top (drain, 100 μm) electrodes, a ~100 nm thick channel, and a side-gate electrode with an area of 1.5 × 1.5 mm^2. The inset shows an optical image of BBL-vOECT. (e) Output characteristics of BBL-vOECT measured in the dark and under illumination (660 nm, 8.7 mW cm^{-2}). V_{DS} was swept from 0 to 0.6 V at rate of 5 mV s^{-1}, with V_{GS} varying from 0 to 0.6 V at a step of 0.1 V. (f) Real-time channel current (I_{DS}) response under varying light intensities (0.9 μW cm^{-2} to 8.7 mW cm^{-2}) measured at V_{DS} = 0.4 V and V_{GS} = 0.4 V. (g) Schematic of photoelectrochemical synaptic device operation. (h) Excitatory postsynaptic current (EPSC) response to ten consecutive light pulses at a frequency of 5 Hz. The paired-pulse facilitation (PPF) index, calculated as A2/A1 × 100%, where A1 and A2 represent the amplitudes of the first and second EPSCs, respectively, quantifies short-term synaptic plasticity. (i) PPF index as a function of light pulse intervals (660 nm, 8.7 mW cm^{-2}, at V_{DS} = V_{GS} = 0.4 V). (j–l) Short-term memory (STM) to long-term memory (LTM) transition modulated by pulse number, frequency, and intensity measured at V_{DS} = V_{GS} = 0.4 V. (m) Learning-forgetting-relearning behavior demonstrating accelerated reacquisition measured at V_{DS} = V_{GS} = 0.4 V.

shift to more negative values, while the reduction peak current and capacitance increase slightly (Figure S3, electrochemical impedance spectroscopy (EIS) measurements with and without light exposure), suggesting that the electron-accepting capability of BBL is further enhanced under light. Under illumination, the open-circuit voltage (V_{OC}) decreases from 260 to 157 mV against an Ag/AgCl reference electrode compared to the dark condition (Figure 2c). Upon light removal, the V_{OC} returns to its original value, with a longer relaxation time than that of the initial voltage drop. This behavior is most likely driven by the interaction of the BBL conjugated backbone with incident photons, which induces the formation of excitons (Figure S4). The dissociation of electrons from these excitons perturbs the V_{OC}, shifting it toward more negative values and highlighting the dynamic photoelectric response of the BBL film.

Building on the observed reversible photovoltage generation, we employed BBL as both the channel and gate material to construct OECTs, aiming to explore its photoresponse characteristics and potential applications in optoelectronic devices. We implemented a side-gate vertical configuration (Figure 2d) using phosphate-buffered saline (PBS) as the electrolyte. The vOECT fabrication

process is illustrated in Figure S5, and details can be found in the Experimental Section. The BBL-vOECT device exhibits typical transistor transfer and output characteristics (Figure 2e and Figure S6). Under positive gate bias, cations from the electrolyte migrate into the channel and electrochemically dope the BBL, increasing its conductivity and enabling enhancement-mode operation. Figure S7 demonstrates that the BBL-vOECT device exhibits excellent reversible electrochemical doping-dedoping behavior in an aqueous environment, with no significant drain current decay observed after 1000 pulse cycles, which is in line with previous reports [36–38]. When illuminating the gate electrode with 660 nm light (8.7 mW cm^{-2} at V_{DS} = 0.4 V), we observed a negative shift in the transfer curve, with the threshold voltage (V_{TH}) decreasing from 0.28 to 0.05 V at V_{DS} = 0.4 V (Figure S8). This shift demonstrates effective optical modulation of channel conductivity. Real-time measurements show that the channel current (I_{DS}) exhibits a roughly 10-fold increase from dark state to illumination at 8.7 mW cm^{-2} (Figure 2f). Notably, the enhanced I_{DS} induced by different light intensities can be effectively retained, highlighting the device's capability to store light information. Operating at a bias of 0.4 V, our device achieves high photosensitivity, exhibiting a noticeable increase in channel conductivity even under ultralow light intensities of 870 nW cm^{-2}. Additionally, the relationship between I_{DS} and light intensity (Figure S9) reveals a maximum responsivity of 1.69×10^4 A W^{-1} at light intensities below 0.05 mW cm^{-2}. To investigate the impact of the BBL photoresponsive gate electrode on device performance, we compared the photocurrent responses with and without the BBL coating on the gate under illumination. The results showed that illuminating the BBL-coated gate increased the I_{DS} 5-fold compared to its dark state (Figure S10), whereas the uncoated gate produced only a 1.2-fold change under the same conditions. This difference clearly confirms that BBL as a gate modification layer can induce more pronounced photocurrent changes under light exposure. The inherent high transconductance of an OECT, which enables the conversion of small variations in gate voltage into substantial responses in channel current, underpins the superior design advantage of implementing sensing functionality at the gate electrode [39]. The current response of the device exhibits wavelength dependence, confirmed by illuminating the gate with LEDs of 455 nm (royal blue), 660 nm (deep red), and 850 nm (infrared) under the same intensity (Figure S11). The greatest stable current increase was observed with deep red light. The royal blue LED caused the second largest change for both BBL and PBBT-Me/BBL vOECTs, exceeding that induced by the infrared LED. However, prolonged exposure to 455 nm for 5 min led to film degradation, attributed to repeated thermal deactivation of excited states. Additionally, light at 660 nm can effectively penetrate the epidermis and dermis layers of human skin, making it more suitable for bioelectronic devices interfacing with tissue [13]. Therefore, considering the material absorption characteristics, device stability, and biological applications, 660 nm was chosen as the light stimulus for the rest of the study.

Based on its retina-like light-sensing ability (Figure 2g), we further investigated the potential of this three-terminal device to emulate visual information storage, extraction, and adaptation in biological systems. For synaptic characterization, we employed light stimuli applied to the gate as presynaptic inputs while monitoring the channel current as the postsynaptic response. Under ten consecutive light pulses at 5 Hz, the device exhibits a significant increase in excitatory postsynaptic current (EPSC) (Figure 2h), highlighting its strong capacity for synaptic-like information storage. This behavior closely mimics biological synapses during repeated nerve impulses, where sequential signals lead to cumulative synaptic strengthening or facilitation. The notable difference in EPSC observed before and after light stimulation indicates the presence of non-volatile photonic memory, which is primarily attributed to light-induced ion trapping within the bulk channel. During light stimulation, ions are inserted into the active layer, creating a stable ion-polymer backbone coupling that persists even after light removal [20]. This stable coupling effectively locks in the electronic state changes, enabling long-term retention of stored information.

In biological synaptic systems, synaptic plasticity is manifested through short-term plasticity (STP) and long-term plasticity (LTP), highlighting the brain's ability to adapt and modify synaptic strength in response to varying activity patterns. We therefore evaluated the synaptic behaviors of our organic photoelectrochemical synapse (OPECS) by assessing paired-pulse facilitation (PPF), a key metric for assessing STP in biological neural systems (Figure S12). The PPF index, defined as the amplitude of the second postsynaptic response (A_2) divided by that of the first (A_1), quantifies this facilitation. By applying light pulses as stimuli and measuring EPSC enhancement, we evaluated the PPF index across frequencies from 0.1 to 100 Hz at a constant duty cycle of 50% (Figure 2i), noting that visual neurons typically fire at frequencies from <1 to ~100 Hz [40]. At a frequency of 100 Hz (5 ms pulse duration and 5 ms interpulse interval), the device achieved a PPF index of 226%, demonstrating an efficient response to high-frequency optical stimulation within the biological firing-rate range.

While STP governs temporary synaptic adjustments, LTP plays a critical role in the formation, retention, and retrieval of memories over extended periods. In biological synaptic systems, the transition from short-term memory (STM) to long-term memory (LTM) occurs through repeated stimulation, where both the frequency and intensity of neural activation modulate the strength of synaptic connections. We successfully emulated this process in our device by demonstrating an STM-to-LTM transition through controlled modulation of light pulse number (Figure 2j), frequency (Figure 2k), and intensity (Figure 2l). Analogous to biological sensory systems, the long-term memory formation in the brain can be achieved by repetitive rehearsal or training. Moreover, the device exhibited an intriguing learning-forgetting-relearning behavior that closely mirrors biological memory systems (Figure 2m). After an initial learning phase requiring 100 pulses and a subsequent period of forgetting, the device showed accelerated relearning, requiring only 48 pulses to return to its original state, a characteristic feature of biological memory where reacquisition of forgotten information occurs more rapidly than initial learning.

2.3 | *p*-type Photoelectrochemical Synaptic Device

To achieve bidirectional synaptic behavior, we next developed a *p*-type photoelectrochemical synapse complementary to the *n*-type BBL device. We synthesized a co-soluble ladder-conjugated

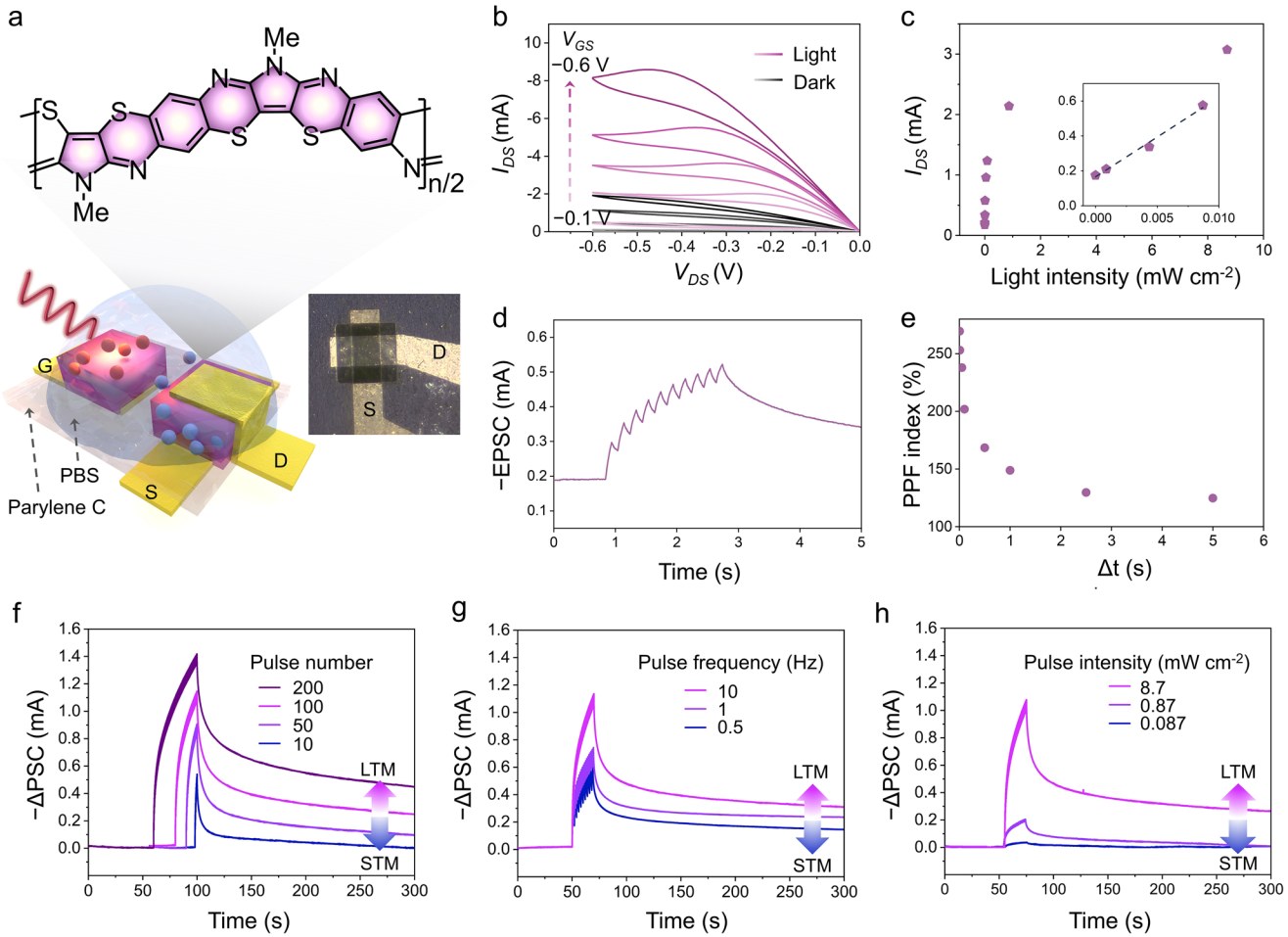

FIGURE 3 | Characterization of PBBT-Me-based *p*-type photoelectrochemical synaptic device. (a) Schematic of PBBT-Me vOECT device configuration, featuring bottom (source, 100 μm) and top (drain, 100 μm) electrodes, a ~100 nm thick channel, and a side-gate electrode with an area of 1.5 × 1.5 mm^2. The inset shows an optical image of PBBT-Me-vOECT. (b) Output characteristics of PBBT-Me vOECT in dark and under 660 nm illumination (8.7 mW cm^{-2}). V_{DS} was swept from 0 to −0.6 V at a rate of −5 mV s^{-1}, with V_{GS} varying from 0 to −0.6 V at a step of −0.1 V. (c) Calibration curve of ***IDS*** versus light intensity under 660 nm illumination (0.9 μW cm^{-2} to 8.7 mW cm^{-2}) measured at V_{DS} = −0.4 V and V_{GS} = −0.4 V. (d) EPSC response to ten successive presynaptic light pulses (8.7 mW cm^{-2}, 5 Hz, V_{DS} = V_{GS} = −0.4 V). (e) PPF index as a function of pulse interval from 5 ms to 5 s (V_{DS} = V_{GS} = −0.4 V). (f–h) STM to LTM transition modulated by light pulse repetition, frequency, and intensity (V_{DS} = V_{GS} = −0.4 V).

polymer, PBBT-Me (Figure 3a), to overcome the acidic solvent limitation of BBL. In situ UV–vis absorption spectroscopy under voltage bias revealed characteristic peaks at 670 and 750 nm, with decreasing absorption intensity under positive bias (Figure S13). This process reflects the partial oxidation of the PBBT-Me polymer, which evolves from its neutral state to an oxidized form. CV curves of PBBT-Me exhibit an oxidation onset potential of +0.32 V versus an Ag/AgCl electrode and show good operational stability, with no significant current degradation observed after 100 consecutive electrochemical doping/dedoping cycles (Figure S14). Similar to the BBL polymer, under light illumination, the oxidation onset of PBBT-Me shifts negatively (by approximately −0.06 V), while its electrochemical performance remains stable without significant changes during 100 consecutive electrochemical doping/dedoping cycles. Additionally, we observed that under light, the capacitance increases slightly (Figure S15) and the V_{OC} of PBBT-Me shifts positively by approximately 250 mV (Figure S16). We speculate that the polymer interacts with incident light to generate excitons, and the resulting delocalized carriers lead to the change in V_{OC}.

We next configured the *p*-type PBBT-Me photonic synapse in a three-terminal vertical transistor architecture, with PBBT-Me serving as both the channel and gate material and PBS as the electrolyte (Figure 3a). Under negative gate voltage, anions from the electrolyte migrate into the channel and electrochemically dope the PBBT-Me polymer, resulting in hole accumulation and an increase in channel current (Figure S17). The device exhibits the typical enhancement-mode behavior, showing increased channel current with increasing gate-source voltage (V_{GS}) and saturation at higher source-drain voltages (V_{DS}) (Figure 3b). Figure S18 shows that the PBBT-Me vOECT device undergoes highly reversible electrochemical doping-dedoping processes in the aqueous electrolyte, with no significant decline in I_{DS} after 1000 pulse cycles. Illumination with 660 nm light shifts the transfer curve positively, decreasing the threshold voltage from −0.20 to −0.08 V at V_{DS} = −0.4 V (Figure S19). I_{DS} increases proportionally with light intensity, achieving a maximum sensitivity of 4.56 × 10^4 mA/(W cm^{-2}) at light intensities below 0.01 mW cm^{-2} (Figure 3c and Figure S20). This high sensitivity indicates efficient photoelectric conversion even under weak illumination.

We subsequently characterized the synaptic behavior of the PBBT-Me-based OPECS device (Figure 3d). Specifically, at a pulse frequency of 100 Hz, the device exhibited a PPF index of 238% (Figure 3e). Additionally, this device demonstrates great STM-to-LTM transition through modulation of light-excitation repetition, frequency, and intensity (Figure 3f–h). Notably, in the case of relearning, only 38 pulses are required following an initial training phase of 100 pulses (Figure S21).

2.4 | Ambipolar Photoelectrochemical Synaptic Transistor

As mentioned earlier, compared to unidirectional synapses, bidirectional synapses that respond to both excitatory and inhibitory inputs are crucial for visual processing and adaptation in neuromorphic systems. Leveraging the excellent and complementary photoresponse capabilities of both BBL and PBBT-Me polymers, we designed a hybrid BHJ device to realize this bidirectional synaptic functionality (Figure 4a). This heterojunction was formed by dissolving PBBT-Me and BBL in methanesulfonic acid (MSA) at various ratios, which were then used as the channel material. We initially evaluated the molecular packing of PBBT-Me: BBL films using grazing-incidence wide-angle X-ray scattering (GIWAXS) (Figure S22 and Table S1). The pristine PBBT-Me and BBL films both predominantly exhibit an edge-on orientation, with strong π–π stacking (010) peaks near q_{xy} = 1.72 Å^{-1} ($d_{\pi-\pi}$ = 3.65 Å). These two films display distinct lamellar peaks at q_z = 0.63 Å^{-1} ($d_{lamellar}$ = 9.97 Å) and q_z = 0.75 Å^{-1} ($d_{lamellar}$ = 8.38 Å), respectively. Additionally, both neat films show broad diffraction peaks near q_z = 1.73 Å^{-1} ($d_{\pi-\pi}$ = 3.63 Å) for PBBT-Me and q_z = 1.55 Å^{-1} ($d_{\pi-\pi}$ = 4.05 Å) for BBL, indicating the presence of a relatively small fraction of face-on stacking in each film. In the PBBT-Me: BBL (1:1) blend, two lamellar diffraction peaks appear at q_z = 0.63 Å^{-1} and q_z = 0.75 Å^{-1}, closely matching those of the individual neat components. The preservation of these lamellar spacings suggests that PBBT-Me and BBL form relatively pure, nanoscale domains with stacking architectures similar to the pure materials. Such formation of non-interfering crystalline domains facilitates efficient hole and electron transport within the BHJ structure. Additionally, we further performed scanning electron microscopy (SEM) to examine the surface morphology of the BHJ film. As shown in Figure S23, a continuous yet rough surface was observed, which increases the contact area between the electrolyte and the channel.

Transfer characteristics demonstrate both *p*- and *n*-channel operation modes (Figure 4b). The unique V-shaped transfer curves are attributed to the simultaneous existence of electron and hole transport within the channel [35]. At a 1:1 blending ratio of PBBT-Me to BBL, the device shows balanced drain current for both *p*- and *n*-type operation, essential for dynamic synaptic applications (Figure S24 and Table S2). The PBBT-Me/BBL heterojunction device exhibits V-shaped transfer characteristics driven by the competing ion doping and dedoping processes. In the *n*-type region (V_{DS} > 0), at V_{DS} = 0.3 V and V_{GS} = 0 V, the negative potential (V_{GD} < 0 V) between gate and drain electrodes causes anions to migrate from the electrolyte into the heterojunction channel, electrochemically doping the PBBT-Me segment and yielding hole-dominant high-conductance (left arm). As V_{GS} is increased gradually, V_{GD} becomes less negative, prompting anions to drift back into the electrolyte and reducing the PBBT-Me doping level, which decreases conductance. Simultaneously, cations (Na^+, K^+) penetrate the channel and electrochemically dope the BBL component, creating concurrent *n*- and *p*-type conduction pathways. When the conductance contributions from both regions balance, the channel reaches its minimum conductance (low-conductance). Further increasing V_{GS} leads to dedoping of PBBT-Me, while BBL doping becomes dominant, enabling electron conduction (right arm). In the *p*-type region, the working mechanism is similar, except that the doping sequence of PBBT-Me and BBL is reversed. We then evaluated the photoresponse of the BHJ OPECS with the 1:1 blending ratio of PBBT-Me to BBL using 660 nm light illumination. Under light exposure, an obvious negative shift in the transfer curves for both *p*- and *n*-type operations was observed (Figure 4c), resulting in increased I_{DS} in the right arm and decreased I_{DS} in the left arm of the V-shaped transfer curves. This bidirectional modulation of conductivity allows the device to generate both excitatory and inhibitory postsynaptic currents (EPSC/IPSC) in response to light pulses under both *p*- and *n*-type conditions. As an example, at V_{DS} = 0.3 V and V_{GS} = 0.4 V, light pulses induce a positive photoresponse current from 130 to 710 μA, indicative of excitatory activity; meanwhile, under the same V_{DS} but with V_{GS} = 0.05 V, the device produces a negative photoresponse current from 130 to 11 μA, demonstrating inhibitory activity. This ability to dynamically switch between excitatory and inhibitory states through optical stimuli highlights its potential for complex neuromorphic functions. Furthermore, both EPSC and IPSC responses are observed under *n*-type and *p*-type operation modes, demonstrating effective optical control of dynamic behavior analogous to biological synapses. The device exhibits both PPF and paired pulse depression, with the peaks of EPSC and IPSC increasing or decreasing upon successive presynaptic spikes for both operation modes (Figure 4d and Figure S25). To benchmark the unique combination of bidirectional optical plasticity and aqueous compatibility achieved in our BHJ OPECS device, we compared its operating voltage and minimum light intensity with those of previously reported optoelectronic synapses based on various device architectures, including OECTs, FETs, and 2D heterojunctions (Figure 4e, Table S3) [4, 13, 15–18, 31, 41–44]. Most existing photonic synapses that support bidirectional plasticity require significantly higher operating voltages (>1 V) [16, 18, 42, 43] and/or strong light input (>1 mW cm^{-2}) [4, 42, 43] and are typically limited to dry or inert environments. In contrast, our device demonstrates excitatory and inhibitory responses under low-intensity illumination (~0.9 × 10^{-3} mW cm^{-2}) and low-bias conditions (±0.4 V), while operating reliably in PBS. The ability to achieve such bidirectional modulation without circuit reconfiguration in an aqueous environment positions our work at the intersection of two critical performance domains: ion-mediated plasticity and optical reconfigurability. This distinguishes our synaptic platform from prior efforts, enabling more biologically relevant operation and simplified system-level integration for neuromorphic visual processing.

This non-volatile, dynamic photoresponse mechanism of our device is fundamentally linked to the light-induced electrochemical doping within the PBBT-Me: BBL *p*-*n* heterojunction. CV measurements of the PBBT-Me: BBL BHJ film in PBS solution (Figure S26) reveal its ambipolar features with stable cycling over 100 charging-discharging cycles, indicating reversible

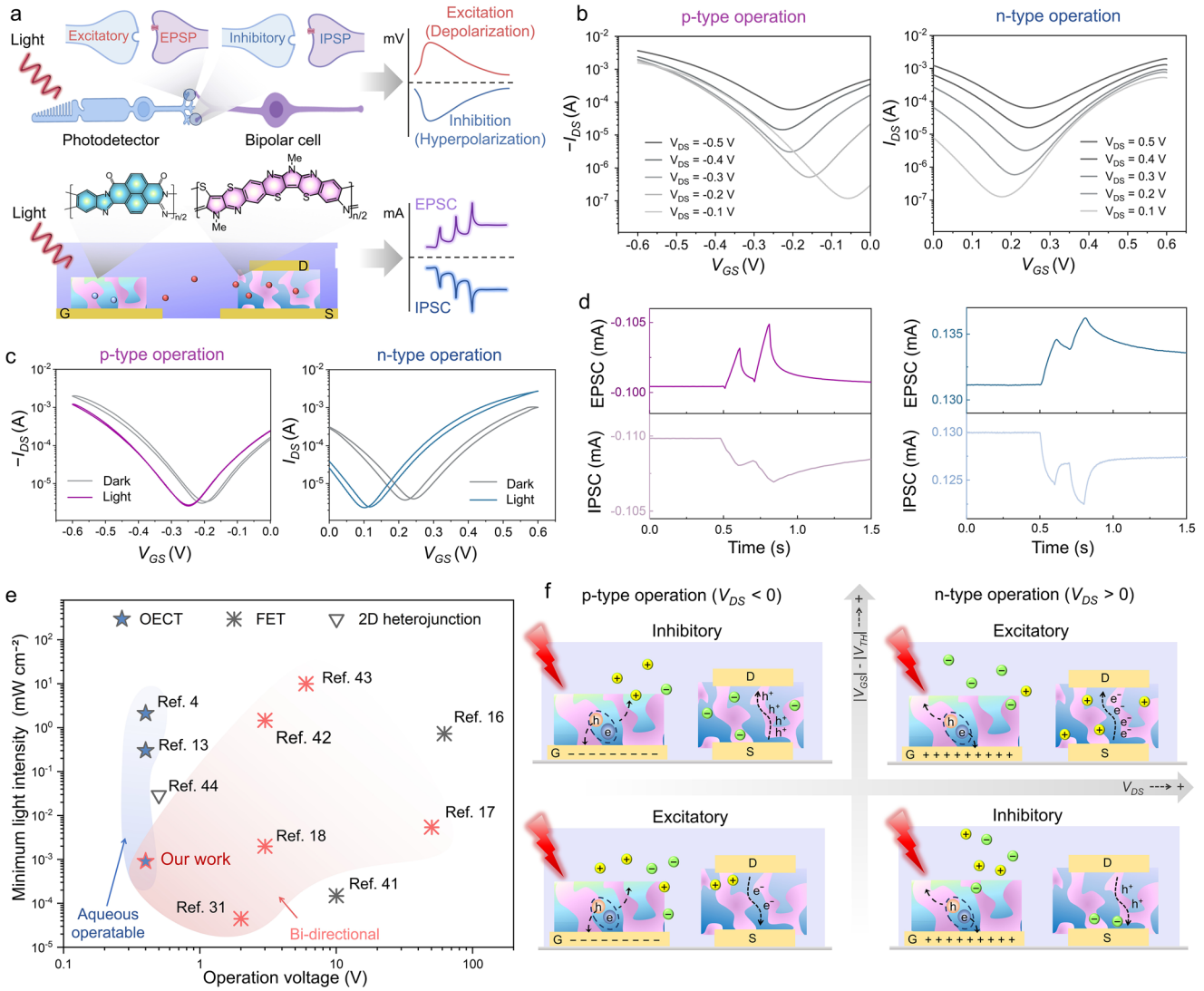

FIGURE 4 | Ambipolar photoelectrochemical synaptic transistor based on PBBT-Me/BBL BHJ vOECTs. (a) Schematic of the biological visual nervous system and its artificial counterpart using PBBT-Me/BBL photosensitive BHJ vOECT, featuring bottom (source, 100 μm) and top (drain, 100 μm) electrodes, a ~100 nm thick channel, and a side-gate electrode with an area of 1.5 × 1.5 mm^2. (b) Transfer characteristics demonstrating ambipolar operation in p- and n-channel modes. (c) Light-induced modulation of transfer characteristics under 660 nm illumination (*p*-type: $V_{DS} = -0.3$ V; *n*-type: $V_{DS} = 0.3$ V). (d) EPSC and IPSC responses to light pulse stimulation (660 nm, 8.7 mW cm^{-2}, 5 Hz). *p*-type EPSC: $V_{GS} = -0.05$ V, IPSC: $V_{GS} = -0.4$ V; *n*-type EPSC: $V_{GS} = 0.4$ V, IPSC: $V_{GS} = 0.05$ V. (e) Performance comparison of optically controlled neuromorphic devices. Scatter plot of minimum light intensity versus operating voltage for various photonic synapse technologies, including OECTs (☆), FETs (*), and 2D heterojunction devices (▽). Blue-shaded region highlights devices operable in aqueous environments, while the red-shaded region denotes devices exhibiting true bidirectional optical plasticity. Stars in red mark our ambipolar BHJ vOECT devices, which uniquely combine low-voltage operation (≤0.4 V), ultralow light intensity requirements (<1 μW cm^{-2}), aqueous compatibility, and both excitatory and inhibitory responses within a single transistor. (f) Schematic illustration of photon-modulated electrochemical doping mechanism underlying the device's dynamic synaptic behavior.

electrochemical redox reactions in aqueous environments. To investigate the electrochemical doping process in the BHJ blend film, in situ UV–vis spectroscopy was employed to monitor the evolution of its absorption spectrum under gradually increasing bias voltages (from 0 to 0.6 V or from 0 to –0.6 V, with a step size of 0.1 V, Figure S27). The results show that, similar to pristine BBL film (Figure S1), when the blend film was doped with cations under negative bias (0 to –0.6 V versus an Ag/AgCl electrode), the absorption peak around 580 nm gradually diminishes, accompanied by the appearance of new features above 700 nm, indicative of polaron formation. Conversely, under positive bias (0 to 0.6 V), when anions are injected, the spectral changes are consistent with the electrochemical doping behavior of the pristine PBBT-Me film (Figure S13), in which the absorption peaks centered at approximately 750 nm gradually weaken, and a broad absorption band appears around 880 nm, attributable to polaron transitions. These findings demonstrate that within the BHJ blend film, the electrochemical doping of each component occurs independently, without interference, enabling effective ion doping in both phases. This ensures efficient charge transport of electrons and holes within their respective pathways, maintaining ambipolar device performance. Furthermore, EIS shows a reduction in charge-transfer resistance under illumination (Figure S28), indicating

efficient photoelectrochemical modulation. Upon light exposure, the BHJ film rapidly generates a positive V_{OC} (versus an Ag/AgCl electrode), which explains the negative shift observed in the transfer curves of the device (Figure 4c). Notably, compared to the individual PBBT-Me or BBL polymers, the BHJ film can sustain its V_{OC} even after light removal, without significant decline, suggesting that the formation of *p-n* heterojunctions stabilizes the excitons generated by illumination (Figure S29). We hypothesize that PBBT-Me, as a donor, absorbs incident light, causing electrons to transition from the highest occupied molecular orbital (HOMO) to the lowest unoccupied molecular orbital (LUMO), forming excitons. These excitons diffuse to the PBBT-Me/BBL interface, where electrons transfer rapidly to BBL (acceptor) because its LUMO level is lower than that of PBBT-Me, while holes remain in PBBT-Me, achieving charge separation. The resulting stable potential difference alters the effective voltage of the gate electrode, prompting corresponding ion migration within the electrolyte, which in turn modulates the device current (Figure 4f). This light-induced positive photovoltage (V_{OC}) shifts the effective gate voltage ($V_{GS,eff}$) to a more positive potential, thereby dictating the bidirectional photoresponse. In the photoinhibition region, corresponding to the left arm of the V-shaped transfer curve, the channel conductance is predominantly governed by the PBBT-Me segment. Under illumination, the effective gate voltage ($V_{GS,eff}$) increases, leading to a decrease in the corresponding V_{GD}. This change promotes the dissociation of anions that were previously coupled with the PBBT-Me backbone, resulting in a reduction in the conductivity of PBBT-Me and consequently a decrease in overall channel conductance, a phenomenon known as photoinhibition. Conversely, in the photoexcitation region, located on the right arm of the V-shaped transfer curve, the channel conductance primarily relies on the BBL component. Under light exposure, the increase in $V_{GS,eff}$ facilitates the penetration of more cations into the channel, which enhances the electrochemical doping of the BBL segment. This process significantly increases overall channel conductance and is characteristic of photoexcitation. Therefore, we define the minimum of the V-shaped transfer curve as the critical threshold marking the transition between the device's optical inhibitory and excitatory responses. When illumination ceases, the injected ions can remain within the channel, maintaining stable coupling with the conjugated backbone of PBBT-Me or BBL polymers. This persistent ion retention facilitates the long-term stability of the photoresponse current, effectively enabling non-volatile memory functionality with a retention time exceeding 130 min (Figure S30). To assess reliability, we conducted repeated light stimulation cycles and monitored the evolution of the synaptic current (Figure S31). The device exhibits stable responses over multiple stimulation cycles, demonstrating excellent endurance behavior. This design strategy, which involves light-induced excitation to generate a stable and sustained potential in the *p-n* heterojunction, is crucial for preserving the device's optical responsiveness over extended periods.

2.5 | Synaptic Arrays for Reprogrammable Image Memory and Erasure

The bidirectional optoelectronic synapse device processes and stores optical information through excitatory and inhibitory functions, advancing the development of adaptive artificial visual systems (Figure 5a). To mimic biological visual processing, we fabricated a 10 × 10 vertically integrated crossbar BHJ OPECS array and evaluated its uniformity by measuring the transfer curves of all 100 devices (Figure S32). The array exhibited consistent electrical performance, demonstrating reliable fabrication and uniform transistor behavior across the entire matrix. In addition, representative pixels across the array demonstrated consistent excitatory photosynaptic responses upon sequential light pulses under both *p*-type and *n*-type operation modes (Figure 5b,c and Figure S33), validating the uniform optical excitability of the array. To evaluate synaptic plasticity, specifically long-term potentiation (LTP) and long-term depression (LTD), we applied 10 consecutive excitatory light pulses followed by 10 inhibitory pulses per cycle, repeated over 10 cycles [45]. Figure 5d,e presents the corresponding conductance modulation during potentiation and depression, respectively. The non-volatile current generated by excitatory pulses was gradually erased using inhibitory pulses, demonstrating reliable and reversible photonic writing and erasing capabilities. To evaluate the LTP/LTD characteristics quantitatively, we extracted the nonlinearity from the characteristic curves (β_P from the LTP curve and β_D from the LTD curve) [46]. The nonlinearity values were β_P/β_D = 2.01/1.42. Throughout the test, the device maintained reliable potentiation and depression behavior without any sign of degradation (Figure S34). This bidirectional conductance modulation mimics key aspects of biological synaptic functions, such as LTP and LTD. The underlying reversible doping and dedoping mechanisms enable flexible conductance modulation and support in situ memory programming and erasure in an aqueous environment. These results lay the foundation for array-level optoelectronic synaptic programmability, where each pixel functions as an independently addressable optoelectronic synapse capable of light-driven memory formation, selective erasure, and in situ reconfiguration, key functionalities for bioinspired visual computing [45, 46].

The photoelectronic synapse replicates the image-recording mechanism of human visual perception through dynamic adjustment of synaptic weights via bidirectional photoresponses. When illuminated with a light stimulus representing the digit "10" (660 nm, 8.7 mW cm^{-2}, V_{GS} = 0.4 V), the synaptic array exhibits elevated currents at the corresponding pixel locations, indicating successful spatial encoding of optical information (Figure 5f). These currents continue to increase after 10 consecutive light pulses (Figure 5g) and remain stable even after light removal, demonstrating robust non-volatile image memory capability (Figure 5h). To further demonstrate adaptability and reconfigurability, we selectively erased the pixel response corresponding to the digit "1" using inhibitory light pulses under V_{GS} = 0.05 V, effectively resetting the synaptic weights at targeted locations (Figure 5i). Subsequent exposure to excitatory pulses enabled optical rewriting of the digit into "8", confirming the array's in situ memory reprogramming functionality (Figure 5j). Benefiting from the vertical crossbar architecture, the effective electrode count per transistor is reduced to approximately 0.3 for a 10 × 10 array, substantially lowering circuit complexity compared to planar configurations, where each transistor typically requires three separate terminals [4]. Additionally, bidirectional optical control of synaptic weights minimizes the need for external electrical gating or multiple control lines, further simplifying the device architecture and enhancing scalability. These results

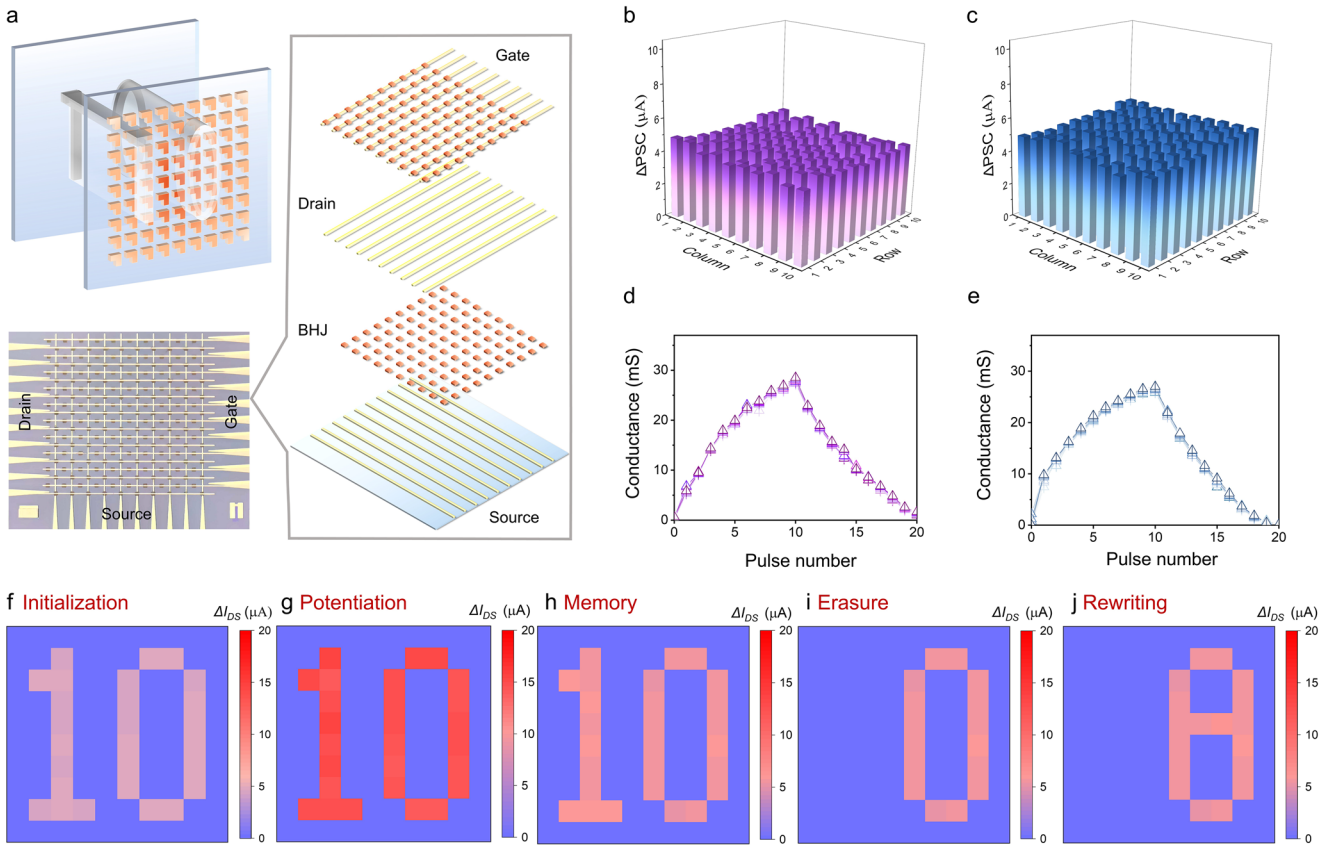

FIGURE 5 | Synaptic array for reprogrammable image memory and erasure. (a) Schematic of a synaptic transistor array for optical pattern recognition. The array features bottom (source, 100 μm) and top (drain, 100 μm) electrodes, a ~100 nm thick channel, and side-gate electrodes with an area of $0.25 \times 0.25\ mm^2$. This array comprises a 10×10 grid of ambipolar BHJ vOECTs, with each transistor acting as a synapse. (b,c) EPSC responses of the transistor array across all pixels in *p*-type and *n*-type operation modes (660 nm, 8.7 mW cm^{-2}, 5 Hz, 10 pulses). (d, e) Potentiation and depression under repeated optical stimulation: 10 excitatory pulses followed by 10 inhibitory pulses per cycle, for 10 cycles (660 nm, 8.7 mW cm^{-2}, 5 Hz), under *p*-type and *n*-type operation, respectively. (f) Current distribution across the array under illumination with a "10"-shaped light pattern. (g) Current mapping after 10 light pulse exposure, showing increased conductance in illuminated pixels. (h) Current retention map 60 s after light removal, demonstrating non-volatile memory. (i) Selective pattern erasure of the digit "1" using localized inhibitory light pulses. (j) Optical rewriting of the digit to form "8," demonstrating in situ memory reconfiguration.

highlight the spatial selectivity and adaptive reconfigurability of the synaptic array, enabling light-driven memory formation, selective erasure, and rewritable image storage. This demonstration paves the way for practical applications in neuromorphic visual perception, pattern recognition, and adaptive artificial vision systems.

2.6 | Image Denoising

The bidirectional response of the BHJ vOECT provides an intrinsic mechanism for in-sensor image preprocessing, minimizing redundant data transfer between sensing and computation units. By exploiting the tunable transition from IPSC to EPSC, the array performs real-time image denoising directly in the device plane. A noisy optical input containing the digit patterns "0, 1, 3, 6, 8" with random background noise was projected onto the 10×10 array (Figure 6a). The initial photocurrent distribution (Figure 6b) was subsequently updated through repeated light-pulse stimulation (Figure 6c–e). For each pulse stage (1, 2, and 10 pulses), the 10×10 grayscale images were partitioned into foreground (digit) and background regions based on the illumination map. Contrast was defined as the normalized difference between the mean foreground and background currents, with the ideal noise-free image set to unity (contrast = 1). As the number of pulses increased, the foreground-background contrast improved monotonically, reaching 0.95 after 10 pulses, demonstrating effective noise suppression and feature enhancement (Figure 6f).

The bidirectional response amplifies foreground-background disparity and mitigates the effect of stochastic noise, improving pattern separability for subsequent visual recognition tasks. To objectively illustrate this improvement, the denoised outputs were further analyzed using a statistical feature-space visualization. A comparative visualization pipeline was built for five-digit classes (0, 1, 3, 6, 8) across four processing stages (initial, 1, 2, and 10 pulses). To mitigate the effect of limited sample size, each 10×10 image underwent lightweight data augmentation (small-angle rotation, sub-pixel translation, mild brightness/contrast jitter, and low-probability blur). These operations expand within-class deformations and noise without altering semantic labels, thereby mimicking typical perturbations in real imaging. Low-frequency coefficients extracted via 2-D Discrete Cosine Transform (DCT) were standardized and embedded into a 2D subspace using Linear

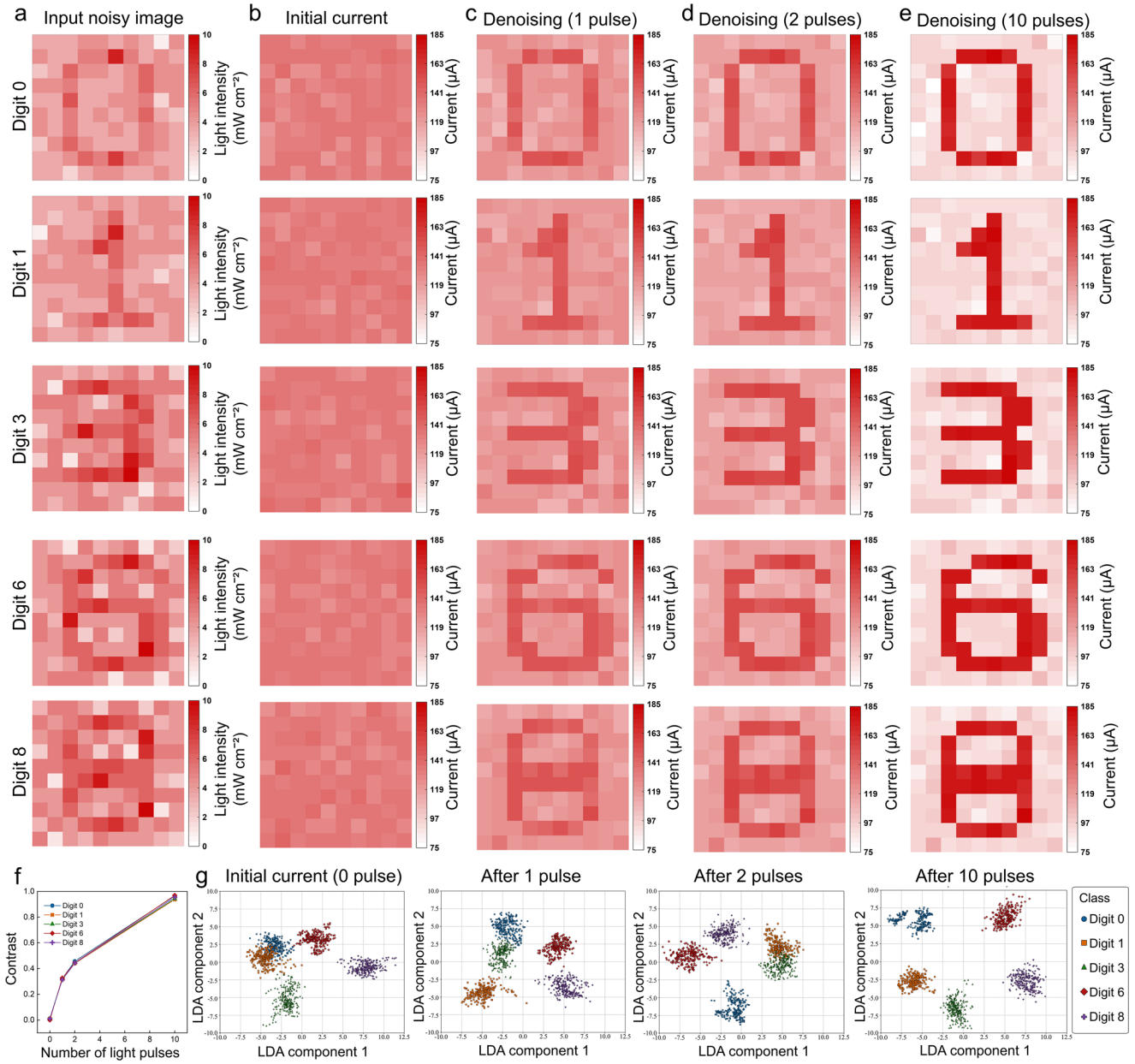

FIGURE 6 | Image denoising based on the bidirectional behavior of the BHJ vOECT. (a) Input noisy image with "0, 1, 3, 6, 8"-shaped patterns, respectively. (b) Initial current of each pixel according to its position. (c-e) Output images after denoising with 1, 2, and 10 pulses, respectively. (f) Contrast enhancement of processed images compared to the noisy input (ideal contrast = 1). (g) Clustering results of digit classes at different processing stages, showing improved class separability after denoising.

Discriminant Analysis (LDA). The LDA projections (Figure 6g) reveal that with increasing pulse number, intraclass clusters become tighter and interclass separation increases, indicating improved feature discriminability and demonstrating the array's hardware-level denoising and feature-enhancement capability.

3 | Conclusion

In summary, we have developed a photoelectrochemical synaptic array based on BHJ vOECTs that achieves light-modulated dynamic photoresponse in an aqueous environment. Inspired by retinal photoreceptors and bipolar cells, our device leverages photo-modulated electrochemical doping and ion interactions to dynamically modulate channel conductivity. Using light patterns as presynaptic inputs, the device demonstrates diverse synaptic functions, including STP and LTP, while enabling STM to LTM transition. The inherent ambipolar behavior of the BHJ vOECTs, exhibiting both depletion and enhancement characteristics in *p*- and *n*-type operations, allows for adaptive photosynapses with both excitatory and inhibitory features in a single device. This dual-function capability effectively simulates ion flux-driven synaptic activity intrinsic to biological systems. Notably, the array demonstrates photo-rewritable functionality, enabling optical writing, erasing, and relearning, without the need for electrical erasure pulses or selector elements. The successful realization of image recognition and denoising using this reprogrammable array, together with its simplified circuitry enabled

by the monolithic vertical architecture and crossbar design, represents a significant advance in artificial visual systems. Building upon this foundational work, future developments will focus on expanding the operational light intensity and wavelength range, improving long-term stability, and integrating with multilayer neuromorphic architectures, further unlocking its potential in intelligent visual processing, human-machine interfaces, robotics, and neuroprosthetics.

4 | Experimental Section

4.1 | Materials

Methanesulfonic acid (MSA), polyphosphoric acid, 2,3-dibromo-N-methylmaleimide, phenylphosphonic acid, Micro-90, BBL (viscosity $\eta = 1.6$ dL g^{-1}), and phosphate-buffered saline (PBS, 137 mM NaCl, 2.7 mM KCl, 10 mM Na_2HPO_4, and 1.8 mM KH_2PO_4) were purchased from Merck. 2,5-diamino-1,4-benzemedithiol dihydrochloride was purchased from Tokyo Chemical Industry (TCI) Chemicals. The *p*-type ladder conjugated polymer, poly[6-methyl-pyrrolo[3,2-b:4,5-b′]bis-[1,4]benzothiazine] (PBBT-Me), was synthesized following our previous report [47] (87% yield, viscosity η = 2.7 dL g^{-1} in MSA at 25°C, molecular weight Mv = 18.6 kDa). The estimation of M_v was calculated using the Mark–Houwink–Sakurada equation ($\eta = K M_v\alpha$, where $K = 5.11 \times 10^{-6}$ g dL^{-1} and $\alpha = 1.34$), and the viscosity was measured using a Ubbelohde viscometer [34, 48]. All chemicals from commercial sources were used without further purification.

4.2 | Device Fabrication

The vertical organic electrochemical transistors (vOECTs) were fabricated using standard photolithography, lift-off, and dry etching processes (as detailed in Figure S5) [49]. Initially, source and gate electrodes (Cr/Au: 5/50 nm) were patterned onto pre-cleaned p-Si/SiO_2 substrates using photolithography and subsequently deposited via thermal evaporation (DE Technology DE400). Next, a 2 μm-thick insulating layer of Parylene C was deposited onto the substrate. Prior to deposition, a dust-free cotton swab soaked in the adhesion promoter 3-(trimethoxysilyl)propyl methacrylate (A-174 Silane) was placed in the deposition chamber to enhance the adhesion of the Parylene C film during the coating process. Subsequently, a dilute Micro-90 detergent solution (10% by weight in deionized water) was spin-coated onto the Parylene C to act as an anti-adhesion layer, facilitating the subsequent peeling process. A second layer of Parylene C was deposited as the sacrificial layer. After the Parylene deposition, the wafer was then coated with a 12 μm-thick AZ P4620 photoresist, which was patterned to delineate the desired channel and gate regions. Reactive ion etching (Oxford Plasmalab80) was employed (at 50 sccm O_2, 10 sccm CHF_3, and 150 W operating conditions) to etch the Parylene C layers, defining the channels and gate structures precisely.

The ladder polymers of BBL and PBBT-Me were dissolved separately in methanesulfonic acid (10 mg/mL) and stirred at 100°C for 3 h. Meanwhile, the ambipolar BHJ solution was prepared by blending 10 mg/ml PBBT-Me and 10 mg/ml BBL solutions at specified ratios, achieving a total concentration of 10 mg/ml. The resulting solution was then spin-coated onto the prepatterned substrates at a spin speed of 1000 r.p.m. for 60 s, followed by a 15 min immersion in an IPA bath to remove the residual MSA. The films were then dried with a nitrogen gun, forming a ∼100 nm-thick photoactive layer in both the channel and gate regions. The sacrificial Parylene C layer was subsequently peeled off, exposing the active regions for the channel and gate. To complete the device, a top drain electrode consisting of 50 nm Au was patterned by photolithography (Figure S5 displays the fabricated vOECT device. Unless otherwise specified, all channels used in this work are equipped with bottom (source, 100 μm) and top (drain, 100 μm) electrodes, a channel thickness of ∼100 nm, and a side-gate electrode with an area of 1.5×1.5 mm^2).

For the synaptic array, a 10×10 matrix of vertical BHJ vOECTs was fabricated in a crossbar configuration. Aside from differences in the sequence of gate electrode fabrication, the overall process closely followed the same steps as those described for the single vOECTs. Unlike individual vOECT fabrication, the array's gate electrodes were deposited last, simultaneously with the drain electrodes. This design simplifies the fabrication of the vertical array while ensuring that each channel is integrated with a dedicated gate electrode (as shown in Figure 5a), maintaining a uniform distance between each gate and its corresponding channel. The array features bottom (source, 100 μm) and top (drain, 100 μm) electrodes, a ∼100 nm thick channel, and side-gate electrodes with an area of 0.25×0.25 mm^2. This smaller gate area, compared to single devices, was deliberately chosen to achieve higher integration density within the array.

4.3 | Electrochemical Characterization

Electrochemical properties of the BBL, PBBT-Me, and PBBT-Me/BBL BHJ films in 1× PBS solution under dark and illuminated conditions were evaluated through cyclic voltammetry (CV) and electrochemical impedance spectroscopy (EIS), performed using a Metrohm Autolab potentiostat in a three-electrode configuration. In the measurements, a saturated Ag/AgCl electrode served as the reference electrode (RE), while a platinum wire functioned as the counter electrode (CE). The films were spin-coated from 10 mg/mL solutions in MSA onto a pre-patterned Cr/Au electrode with a 2 μm-thick Parylene C layer acting as an insulator to prevent direct contact between the electrolyte and the metal electrodes (serving as the working electrode, WE). CV scans were conducted at a rate of 50 mV/s. EIS measurements covered a frequency range from 10^4 to 10^{-1} Hz, using a 10 mV sinusoidal signal. The volumetric capacitance (C*) was calculated by dividing the measured capacitance C by the volume (V) of the deposited film [37].

UV–visible spectra were measured with an Agilent Cary 5000 UV–visible NIR spectrophotometer. Subsequently, in situ spectroelectrochemistry measurements were performed under a constant offset bias range of 0 to −0.6 V for BBL, 0 to 0.6 V for PBBT-Me, and −0.6 to 0.6 V for PBBT-Me: BBL films versus Ag/AgCl electrode operated in PBS aqueous electrolyte. The absorption spectra were recorded over the wavelength range of 350 to 950 nm for biased films. The thickness of the polymer films was characterized by Alpha-Step profilemeter (KLA-Tenc.). Scanning electron microscopy (SEM) imaging was performed using a

Zeiss GeminiSEM 360 microscope. The Grazing-incidence Wide-Angle X-ray Scattering (GIWAXS) experiment was conducted using a Xenocs Xeuss 3.0 instrument equipped with a Cu Kα X-ray source (λ = 1.54 Å) and a Dectris Eiger 500K detector. The measurement was performed at a fixed grazing-incidence angle of 0.2°.

4.4 | Electrical Characterization

The current-voltage characteristics were performed on a Keithley B1500, with 1x PBS solution as the electrolyte. The threshold voltages of all vOECTs were extracted from a fit of the linear portion of the $\sqrt{I_D}$ versus V_{GS} curves. We monitored the real-time changes in the channel current of the vOECT at a constant V_{DS} and V_{GS}. After achieving a stable baseline, light stimulation was applied using a Thorlabs DC2200 LED driver and M660L4 LED (660 nm). Each synaptic transistor was individually tested using a droplet of 1x PBS electrolyte.

4.5 | Statistical Analysis

Statistical analyses of the experimental results are presented as mean ± standard deviation (SD), with a minimum of three independent replicates ($n \geq 3$), unless otherwise noted in the figure captions.

Author Contributions

X.S., X.W., and C.W. conceived and designed the experiments. X.S. and X.W. conducted the experiments, collected the data, and performed the initial analysis. H.W. and W.L. performed the image denoising. B.X. helped with the electrical characterization of devices. J.T. assisted with electrochemical characterization. Z.L. and K.R. contributed to the image recognition. Q.H. and J. L. characterized the two materials. All the authors discussed the results and contributed to the manuscript preparation. X.S., X.W., L.Y., Y.L., S.Z., T.L., and C.W. wrote the manuscript.

Acknowledgements

This research is supported by the National University of Singapore Presidential Young Professorship, A*STAR under its RIE 2025 Human Health and Potential FY22 Prenatal/Early Childhood Grant Call (Award H23P1M0003), the Ministry of Education, Singapore under its Academic Research Fund, and the Tsinghua-NUS Joint Research Initiative Fund Award.

Conflicts of Interest

The authors declare no conflicts of interest.

Data Availability Statement

The data that support the findings of this study are available from the corresponding author upon reasonable request.

References

1. H. Chen, Y. Cai, Y. Han, and H. Huang, "Towards Artificial Visual Sensory System: Organic Optoelectronic Synaptic Materials and Devices," *Angewandte Chemie International Edition* 63 (2024): 202313634, https://doi.org/10.1002/anie.202313634.

2. H. Shim, F. Ershad, S. Patel, et al., "An Elastic and Reconfigurable Synaptic Transistor based on a Stretchable Bilayer Semiconductor," *Nature Electronics* 5 (2022): 660–671, https://doi.org/10.1038/s41928-022-00836-5.

3. Y. Wang, Z. Lv, J. Chen, et al., "Photonic Synapses Based on Inorganic Perovskite Quantum Dots for Neuromorphic Computing," *Advanced Materials* 30 (2018): 1802883, https://doi.org/10.1002/adma.201802883.

4. K. Chen, H. Hu, I. Song, et al., "Organic Optoelectronic Synapse Based on Photon-Modulated Electrochemical Doping," *Nature Photonics* 17 (2023): 629–637, https://doi.org/10.1038/s41566-023-01232-x.

5. W. W. Lee, Y. J. Tan, H. Yao, et al., "A Neuro-Inspired Artificial Peripheral Nervous System for Scalable Electronic Skins," *Science Robotics* 4 (2019): 2198, https://doi.org/10.1126/scirobotics.aax2198.

6. W. Heng, S. Solomon, and W. Gao, "Flexible Electronics and Devices as Human–Machine Interfaces for Medical Robotics," *Advanced Materials* 34 (2022): 2107902, https://doi.org/10.1002/adma.202107902.

7. Z. He, H. Duan, J. Zeng, et al., "Perovskite Retinomorphic Image Sensor for Embodied Intelligent Vision," *Science Advances* 11 (2025): 2834, https://doi.org/10.1126/sciadv.ads2834.

8. Z. Wang, T. Wan, S. Ma, and Y. Chai, "Multidimensional Vision Sensors for Information Processing," *Nature Nanotechnology* 19 (2024): 919–930, https://doi.org/10.1038/s41565-024-01665-7.

9. Z. Zhang, S. Wang, C. Liu, R. Xie, W. Hu, and P. Zhou, "All-in-One Two-Dimensional Retinomorphic Hardware Device for Motion Detection and Recognition," *Nature Nanotechnology* 17 (2022): 27–32, https://doi.org/10.1038/s41565-021-01003-1.

10. P. A. Merolla, J. V. Arthur, R. Alvarez-Icaza, et al., "A Million Spiking-Neuron Integrated Circuit With a Scalable Communication Network and Interface," *Science* 345 (2014): 668–673, https://doi.org/10.1126/science.1254642.

11. H. Tan, Z. Ni, W. Peng, et al., "Broadband Optoelectronic Synaptic Devices Based on Silicon Nanocrystals for Neuromorphic Computing," *Nano Energy* 52 (2018): 422–430, https://doi.org/10.1016/j.nanoen.2018.08.018.

12. M. Lee, W. Lee, S. Choi, et al., "Brain-Inspired Photonic Neuromorphic Devices using Photodynamic Amorphous Oxide Semiconductors and their Persistent Photoconductivity," *Advanced Materials* 29 (2017): 1700951, https://doi.org/10.1002/adma.201700951.

13. V. Druet, D. Ohayon, C. E. Petoukhoff, et al., "A Single *n*-type Semiconducting Polymer-Based Photo-Electrochemical Transistor," *Nature Communications* 14 (2023): 5481, https://doi.org/10.1038/s41467-023-41313-7.

14. D. Attwell and S. B. Laughlin, "An Energy Budget for Signaling in the Grey Matter of the Brain," *Journal of Cerebral Blood Flow & Metabolism* 21 (2001): 1133–1145, https://doi.org/10.1097/00004647-200110000-00001.

15. S. Wang, C. Chen, Z. Yu, et al., "A MoS_2/PTCDA Hybrid Heterojunction Synapse With Efficient Photoelectric Dual Modulation and Versatility," *Advanced Materials* 31 (2019): 1806227, https://doi.org/10.1002/adma.201806227.

16. J. Yu, X. Yang, G. Gao, et al., "Bioinspired Mechano-Photonic Artificial Synapse Based on Graphene/MoS_2 Heterostructure," *Science Advances* 7 (2021): 9117, https://doi.org/10.1126/sciadv.abd9117.

17. X. Zhu, Y. Yan, L. Sun, et al. *Advanced Materials* 34 (2022): 1.

18. X. Pang, Y. Wang, Y. Zhu, et al., "Non-Volatile Rippled-Assisted Optoelectronic Array for All-Day Motion Detection and Recognition," *Nature Communications* 15 (2024): 1613.

19. P. C. Harikesh, C. Y. Yang, H. Y. Wu, et al., "Ion-Tunable Antiambipolarity in Mixed Ion–Electron Conducting Polymers Enables Biorealistic Organic Electrochemical Neurons," *Nature Materials* 22 (2023): 242–248, https://doi.org/10.1038/s41563-022-01450-8.

20. X. Ji, B. D. Paulsen, G. K. K. Chik, et al., "Mimicking Associative Learning Using an Ion-Trapping Non-Volatile Synaptic Organic Electrochemical Transistor," *Nature Communications* 12 (2021), 2480.

21. Z. Laswick, X. Wu, A. Surendran, et al., "Tunable Anti-Ambipolar Vertical Bilayer Organic Electrochemical Transistor Enable Neuromorphic Retinal Pathway," *Nature Communications* 15 (2024): 6309, https://doi.org/10.1038/s41467-024-50496-6.

22. X. Liu, D. Wang, W. Chen, et al., "Optoelectronic Synapses With Chemical-Electric Behaviors in Gallium Nitride Semiconductors for Biorealistic Neuromorphic Functionality," *Nature Communications* 15 (2024): 7671, https://doi.org/10.1038/s41467-024-51194-z.

23. A. Nawaz, Q. Liu, W. L. Leong, K. E. Fairfull-Smith, and P. Sonar, "Organic Electrochemical Transistors for In Vivo Bioelectronics," *Advanced Materials* 33 (2021): 2101874, https://doi.org/10.1002/adma.202101874.

24. B. D. Paulsen, K. Tybrandt, E. Stavrinidou, and J. Rivnay, "Organic Mixed Ionic–Electronic Conductors," *Nature Materials* 19 (2020): 13–26, https://doi.org/10.1038/s41563-019-0435-z.

25. P. Gkoupidenis, Y. Zhang, H. Kleemann, et al., "Organic Mixed Conductors for Bioinspired Electronics," *Nature Reviews Materials* 9 (2023): 134–149, https://doi.org/10.1038/s41578-023-00622-5.

26. S. Wang, X. Chen, C. Zhao, et al., "An Organic Electrochemical Transistor for Multi-Modal Sensing, Memory and Processing," *Nature Electronics* 6 (2023): 281–291, https://doi.org/10.1038/s41928-023-00950-y.

27. P. C. Harikesh, C. Y. Yang, D. Tu, et al., "Organic Electrochemical Neurons and Synapses with Ion Mediated Spiking," *Nature Communications* 2022, 13, 901.

28. S. Chen, Z. Zhou, K. Hou, et al., "Artificial organic Afferent Nerves Enable Closed-Loop Tactile Feedback for Intelligent Robot," *Nature Communications* 15 (2024): 7056, https://doi.org/10.1038/s41467-024-51403-9.

29. X. Zhang, C. Wang, Q. Sun, et al., "Inorganic Halide Perovskite Nanowires/Conjugated Polymer Heterojunction-Based Optoelectronic Synaptic Transistors for Dynamic Machine Vision," *Nano Letters* 24 (2024): 4132–4140, https://doi.org/10.1021/acs.nanolett.3c05092.

30. Y. Wang, W. Shan, H. Li, et al., "Electronic Structure Formed by Y2O3-Doping in Lithium Position Assists Improvement of Charging-Voltage for High-Nickel Cathodes," *Nature Communications* 16 (2025): 1, https://doi.org/10.1038/s41467-024-52768-7.

31. X. Han, J. Tao, Y. Liang, et al., "Ultraweak Light-Modulated Heterostructure With Bidirectional Photoresponse for Static and Dynamic Image Perception," *Nature Communications* 15 (2024): 10430, https://doi.org/10.1038/s41467-024-54845-3.

32. X. Zhu, C. Gao, Y. Ren, et al., "High-Contrast Bidirectional Optoelectronic Synapses based on 2D Molecular Crystal Heterojunctions for Motion Detection," *Advanced Materials* 35 (2023): 2301468, https://doi.org/10.1002/adma.202301468.

33. S. Fabiano, P. C. Harikesh, H.-Y. Wu, C.-Y. Yang, and D. Tu *Science Advances* 11 (2025): adv3194.

34. H. Y. Wu, J. Da Huang, S. Y. Jeong, et al., "Stable Organic Electrochemical Neurons based on *p*-Type and *n*-Type Ladder Polymers," *Materials Horizons* (2023), 10, 4213–4223.

35. X. Wu, T. L. D. Tam, S. Chen, et al., "All-Polymer Bulk-Heterojunction Organic Electrochemical Transistors With Balanced Ionic and Electronic Transport," *Advanced Materials* 34 (2022): 2206118, https://doi.org/10.1002/adma.202206118.

36. X. Wang, Z. Zhang, P. Li, et al., "Ultrastable *n*-Type Semiconducting Fiber Organic Electrochemical Transistors for Highly Sensitive Biosensors," *Advanced Materials* 36 (2024): 2400287, https://doi.org/10.1002/adma.202400287.

37. H. Sun, M. Vagin, S. Wang, et al., "Complementary Logic Circuits Based on High-Performance *n*-Type Organic Electrochemical Transistors," *Advanced Materials* 30 (2018): 1704916, https://doi.org/10.1002/adma.201704916.

38. J. Surgailis, A. Savva, V. Druet, et al., "Mixed Conduction in an *n*-Type Organic Semiconductor in the Absence of Hydrophilic Side-Chains," *Advanced Functional Materials* 31 (2021): 2010165, https://doi.org/10.1002/adfm.202010165.

39. F. Torricelli, D. Z. Adrahtas, Z. Bao, et al., "Electrolyte-Gated Transistors for Enhanced Performance Bioelectronics," *Nature Reviews Methods Primers* 1 (2021): 66, https://doi.org/10.1038/s43586-021-00065-8.

40. F. Li, D. Li, C. Wang, et al., *Nature Communications* 2024, 15, 1.

41. B. Pradhan, S. Das, J. Li, et al., "Ultrasensitive and Ultrathin Phototransistors and Photonic Synapses Using Perovskite Quantum Dots Grown From Graphene Lattice," *Science Advances* 6 (2020): 5225, https://doi.org/10.1126/sciadv.aay5225.

42. J. Fu, C. Nie, F. Sun, G. Li, H. Shi, and X. Wei, "Bionic Visual-Audio Photodetectors with In-Sensor Perception and Preprocessing," *Science Advances* 10 (2024): 8199, https://doi.org/10.1126/sciadv.adk8199.

43. X. Hong, Y. Huang, Q. Tian, et al., "Two-Dimensional Perovskite-Gated AlGaN/GaN High-Electron-Mobility-Transistor for Neuromorphic Vision Sensor," *Advanced Science* 9 (2022): 2202019, https://doi.org/10.1002/ADVS.202202019.

44. S. Feng, J. Li, L. Feng, et al., "Dual-Mode Conversion of Photodetector and Neuromorphic Vision Sensor via Bias Voltage Regulation on a Single Device," *Advanced Materials* 35 (2023): 2308090, https://doi.org/10.1002/adma.202308090.

45. Y. Choi, S. Oh, C. Qian, J. H. Park, and J. H. Cho, "Vertical Organic Synapse Expandable to 3D Crossbar Array," *Nature Communications* 11 (2020): 4595.

46. S. Seo, B. S. Kang, J. J. Lee, et al., "Artificial Van Der Waals Hybrid Synapse and its Application to Acoustic Pattern Recognition," *Nature Communications* 11 (2020): 3936.

47. Q. He, J. Wang, T. L. Dexter Tam, et al., "Thermoelectric Performance Enhancement of p -Type Pyrrolo[3,2-b:4,5-b′]bis[1,4]benzothiazine Conjugated Ladder Polymer by Pendant Group Engineering," *ACS Materials Letters* 5 (2023): 2829–2835, https://doi.org/10.1021/acsmaterialslett.3c00758.

48. H. Y. Wu, C. Y. Yang, Q. Li, et al., "Influence of Molecular Weight on the Organic Electrochemical Transistor Performance of Ladder-Type Conjugated Polymers," *Advanced Materials* 34 (2022): 2106235, https://doi.org/10.1002/adma.202106235.

49. W. Huang, J. Chen, Y. Yao, et al., "Vertical Organic Electrochemical Transistors For Complementary Circuits," *Nature* 613 (2023): 496–502, https://doi.org/10.1038/s41586-022-05592-2.

Supporting Information

Additional supporting information can be found online in the Supporting Information section.

Supporting File: adma72961-sup-0001-SuppMat.docx.